Euler–Lagrange approach to investigate respiratory anatomical shape effects on aerosol particle transport and deposition

Mohammad S Islam[1,2], Suvash C Saha[1], Emilie Sauret[2],
Hui Ong[3], Paul Young[3], and YT Gu[2]

Abstract

An accurate knowledge of the pulmonary aerosol particle transport in the realistic lung is essential to deliver the therapeutic particle to the targeted site of the bifurcating airways. The available *in silico* studies have enriched the knowledge of the aerosol transport and deposition (TD) in the lung; however, the absolute TD data in the realistic lung airway are still elusive. Therefore, in this study, a 3-D geometry of the human lung central airway is developed from the computed tomography (CT) images. A CT scan-based modified lung geometry with a smooth surface and nonrealistic Weibel's lung geometry is also generated. The coal mine exhausted aerosol TD in the upper airway is investigated. The Euler–Lagrange (E-L) method for particle tracking and ANSYS Fluent solver are used to carry out the entire investigation. The effective diameter method is employed to define the shape-specific particles and is integrated with the E-L method. The anatomical shape effects on the deposition patterns are investigated for different deposition parameter. The numerical results illustrated that the airway geometry, particle shape, particle diameter, and breathing flow rates significantly influence the aerosol TD pattern in the upper airway. The present study reports that airway tracheal wall is the new deposition hot spot for the CT-based geometry instead of bifurcating area for the idealized model, which might be helpful for zone-specific drug delivery to the respiratory airways.

Keywords

Deposition hot spot, particle shape, anatomical shape, drug delivery, pharmaceutical aerosol

Introduction

Since the beginning of the industrial revolution, there is a significant increase in power plant and motor vehicle usage. Consequently, air pollution has increased significantly over the past few centuries. The inhaled air (air inhaled by humans) accommodates a large percentage of suspended aerosols, liquid as well as solid, organic substances, and bacteria.[1] In the case of inhalation, nasal cavities and oropharyngeal airways act as a filter. Most of the inhaled micron particles deposit in the nasal cavities and oral region during the inhalation process due to turbulent dispersion and inertial impaction. The remaining (smaller) particles pass through the trachea and deposit in the bronchi and alveoli.[1] The deposition pattern in lung is attributable

[1] School of Mechanical and Mechatronic Engineering, University of Technology Sydney, Sydney, NSW, Australia
[2] School of Chemistry, Physics & Mechanical Engineering, Queensland University of Technology, Brisbane, QLD, Australia
[3] Respiratory Technology, Woolcock Institute of Medical Research and Discipline of Pharmacology, The University of Sydney, Sydney, NSW, Australia

Corresponding author:
Suvash C Saha, School of Mechanical and Mechatronic Engineering, University of Technology Sydney, Sydney, NSW, Australia.
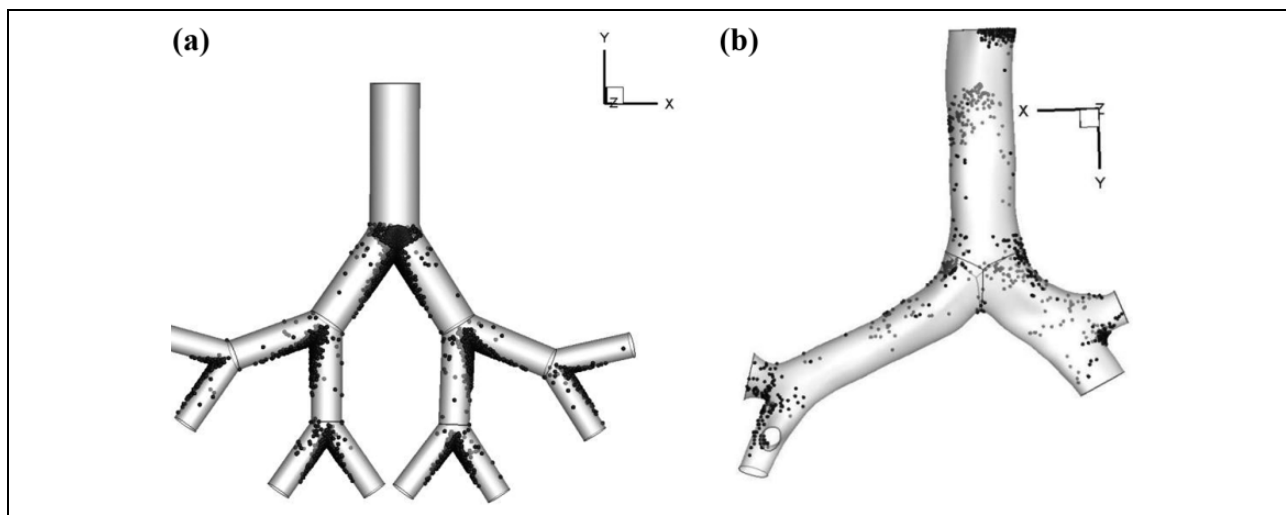Email: suvash.saha@uts.edu.au

Figure 1. Deposition pattern in a G1–G3 model: (a) idealized and (b) CT-based realistic model. CT: computed tomography.

to biological and physical factors. The biological factor includes lung geometrical structure, different breathing pattern, and viscous mucus layer and periciliary layer. On the other hand, physical factor includes fluid–particle dynamics, fluid dynamics, particle physical properties, and different retention mechanisms. According to the published literature, the first approach to simulate the dust particle physical parameters effects on particle transport and deposition (TD) in the upper bronchiole is studied by Watson.[2] A theoretical study investigates aerosol TD in the human bifurcating airways and reports minimum deposition for 0.3 mm diameter particle.[3]

The available published studies have adopted different particle tracking methods. The Lagrangian particle tracking and Eulerian particle tracking methods are the two main approaches to simulate particle TD numerically. Investigating the particles deposition pattern in the lung is challenging because of the highly complex anatomical arrangement of the lung.[3–7] Aslett et al.[8] developed a scale diagram of the respiratory airways; the study described the lung volume and subdivisions of the respiratory tract for a healthy man. Briscoe and Dubois[9] investigated the dimensions of the human lung and airway resistance based on different age and body size.

The most comprehensive and simple human lung geometry was defined by Weibel.[3] Weibel's study clearly explained the dimensions between the parent and daughter branches. Horsfield and Cumming[10] have proposed more practical lung geometry compared to Weibel's, the study reports that the daughter branches diameters are not identical. Raabe et al.[11] have developed an asymmetric lung model. Some geometrical developments of the idealized lung model have been conducted to overcome its complexity.[11,12] Koblinger et al.[13] proposed a stochastic lung model to investigate the particle TD in the tracheobronchial airway, and the study used Monte Carlo technique to the random walk of the particle. Balásházy and Hofmann[14] used

Monte Carlo technique to simulate the inspiratory flow. The results showed that the bifurcation zone is the hot spot for foreign particle deposition. Realistic deposition models have also been employed to accurately examine the actual particle TD patterns in a human lung.[15,16] Cebral and Summers[17] have investigated the pressure and flow pattern for tracheal, and central bronchial in the anatomically realistic model and their investigation concluded that pressure decreased and shear stress increased in the stenosis part. Kvasnak and Ahmadi[18] have numerically studied unsteady airflow in a human lung computed tomography (CT) scan geometry. They have shown the velocity distribution and variation of air vorticity in the lung.

A range of published literatures has been performed to examine the deposition pattern of spherical aerosol particles in a nonrealistic and realistic geometry.[1,19–25] As the suspended particles are mostly nonspherical (NS) in size,[26] it is necessary to investigate the NS aerosol TD in the lung airway. Kasper[27] has studied the dynamics and measurement of the NS smoke particle. Wen and Kasper[28] have studied the drag and orientation of chain aggregates for NS particle. Kasper and Wen[29] has studied relative measurement as a function of submicron particle aggregates. Fan and Ahmadi[30] conducted a sublayer smooth wall model for ellipsoidal aerosol particle transport by employing the motion of the ellipsoidal particles. Zhang et al.[31] have studied the NS particle (ellipsoidal) TD in turbulent channel flow. A review study has been conducted by Kleinstreuer and Feng[32] on NS particle TD. They have reviewed theories for both spherical and NS particle TD in shear flow. Recently, a comprehensive review study has been conducted by Zhong et al.[33] for computational fluid dynamics (CFD)-discrete element method (DEM) modeling of NS particle and the representation of the NS particle is presented. In reality, during inhalation, particles can collide with each other, although most of the published study ignored the particle–particle collision

effects for lung deposition. However, if the particle suspension entering the tracheobronchial airway is dilute, then direct particle interactions can be ignored. The deposition pattern in a realistic human lung and the deposition pattern for available *in silico* model should be significantly different due to the different anatomical shape. A comprehensive comparative study of the various anatomical shape geometry is essential for proper understanding of the pharmaceutical aerosol deposition pattern in the human airways.

In this study, a numerical framework for spherical and NS particle has been developed to examine the micron diameter particle TD in the central bronchiole of the lung. Different lung geometries are used to investigate the anatomical shape effects on particle TD. To inquire into the realistic aerosol particle TD pattern in the human airway, CT-based airway model has been generated. A comprehensive study for grid refinement and model validation is conducted. Moreover, an extensive parametric study has been carried out for particle TD for different deposition parameters for spherical and NS particles. The deposition pattern for idealized and CT-based lung model is shown in Figure 1.

Numerical methods

In the current study, a three-dimensional (3-D), pressure-based solver and double precision serial processing model are used. ANSYS Fluent solver and Lagrangian approach are used for the numerical simulation. The following mass and momentum equations are solved.

$$\frac{\partial \rho}{\partial t} + \nabla \cdot (\rho \vec{v}) = S_m \tag{1}$$

where S_m is the source term of mass.

$$\frac{\partial}{\partial t}(\rho \vec{v}) + \nabla \cdot (\rho \vec{v}\vec{v}) = -\nabla p + \nabla \cdot \left(\mu\left[(\nabla \vec{v} + \nabla \vec{v}^T) - \frac{2}{3}\nabla \cdot \vec{v}I\right]\right) + \rho \vec{g} + \vec{F} \tag{2}$$

where p is fluid pressure, $\rho\vec{g}$ is gravitational body force, μ is the viscosity, and $\vec{F}$ is external body force. The standard k–ω turbulence model is used as a viscous model. The air density is 1.225 kg/m^3 and viscosity is 0.00001789 kg/m-s used for the present study. The particle equation which is solved for the particle transport can be written as:

$$\frac{d\vec{u}_p}{dt} = F_D(\vec{u} - \vec{u}_p) + \frac{\vec{g}(\rho_p - \rho)}{\rho_p} + \vec{F} \tag{3}$$

where $\vec{F}$ is the force per unit particle mass, $F_D(\vec{u} - \vec{u}_p)$ is the drag force and

$$F_D = \frac{18\mu}{\rho_p d_p^2}\frac{C_D R_e}{24}$$

$\vec{u}$ is the fluid velocity, $\vec{u}_p$ is the particle velocity, μ is fluid, ρ is density of fluid molecular viscosity, ρ_p is the particle density, and d_p is the particle diameter. The relative Reynolds number can be define as

$$R_e \equiv \frac{\rho d_p |\vec{u}_p - \vec{u}|}{\mu} \tag{4}$$

To introduce the NS particle, the effective diameter method (EDM)[34] is used and coupled with Euler–Lagrange method. In EDM, NS particle is deliberated as a spherical particle. In the present study, drag coefficient correlation is used to introduce the NS particle. A shape factor value is incorporated with the correction of drag and lift coefficient. Wadell[35] presented the concept of sphericity. The ratio of the surface area (A_s) of a sphere to the surface area of a particle (A_p) can be defined as the shape factor (ψ). The surface area A_s is equivalent to the volume of particle V_p

$$\psi = \frac{A_s}{A_p} = \frac{\pi^{\frac{1}{3}}(6V_p)^{\frac{2}{3}}}{A_p} \tag{5}$$

Spherical particles have sphericity of 1 whereas NS particles have values less than 1. For a tetrahedron particle, the volume of a tetrahedron is $\frac{\sqrt{2}}{12}s^3$, and the area of a tetrahedron is $\sqrt{3}s^2$. Therefore, equation (5) can be written as:

$$\psi = \frac{\pi^{\frac{1}{3}}\left(6 \cdot \frac{\sqrt{2}}{12}s^3\right)^{\frac{2}{3}}}{\sqrt{3}s^2} \tag{6}$$

The flow is calculated by incorporating the coal particle with the density of 1.55 gm/cm^3 and the aerosol particle is nonevolving. It is evident that the coal mine exhaust particles cause interstitial respiratory diseases.[36] The SIMPLE scheme for pressure–velocity coupling[37] is used in the numerical modeling. To initialize the solution, hybrid initialization technique in discrete phase model (DPM) is used. Hybrid initialization solves Laplace's equations incorporating proper boundary conditions to create the velocity flow field that conforms to highly asymmetric geometrical models and the pressure field to append the fluctuate pressure in the complex computational domain. The inlet velocity and outlet pressure boundary[24,38,39] conditions are used to solve the particle transport, deposition and skip. Additionally, various air flow rates are used to show different breathing conditions. A stationary wall motion and no-slip shear condition are used as a wall condition. The 'trap' boundary condition is used for the DPM.[40–42] The boundary condition 'trap' means the particle will stack on the wall as soon as the particle hits the airway wall. This is a realistic condition because in the real case, human lung mucus is highly sticky and particle is trapped once contact with the mucus layer. The FLUENT user define function (UDF), and MATLAB code are used to track the particles physical location and their interactions with the wall domain. MATLAB code is also used to determine the specific zone deposition of the spherical and the NS particle.

The injection properties have been introduced for the microparticle injection in DPM. We have also used the inlet surface nodes to release the particles, considering every face of the tracheal inlet will release a particle. The particle initial distribution at the inlet surface is uniform and an equal air velocity is employed at the injection site. A velocity inlet boundary condition is used for the single bifurcation model. This study used monodispersed size particle, and all of the particles are introduced at once. The particles are injected at the beginning of the simulation. The particles number concentration is 4.1396×10^7 particles/m^3 and the mass concentration of 1-μm diameter particle is 33.5968 μg/m^3. Morawska et al.[43] investigated the detail particle mass concentration in residential houses in Brisbane during indoor activities conditions and found the mass concentration during indoor activities was 15.5 ± 7.9 μg/m^3. Israel et al.[44] found the average mass concentration of a rural control site was 39 μg/m^3. The particle mass concentration varies depending on specific site and pollutions. The particle concentration value in the present study is in the range of realistic particle concentration values. The present manuscript did not consider the particle–particle interaction. However, the interaction of the continuous phase with the discrete phase has been performed. The particle–particle interaction is necessary when the volume concentration is greater than 15% and in reality, it is nearly impossible to reach 15% volume concentration for lung. Particle–particle interaction during the particle–gas flow can be neglected if the particles become dilute.[45] The collision-free flow corresponds to the dilute phase and particle–particle interaction can be neglected for particle transport in the human lung. Moreover, almost all of the published literature neglect the particle–particle interaction effects for human lung modeling. The average run time for the present simulation was approximately 92 h. A SGI Altix XE Cluster and 960xE5-2680v3@2.5 GHz 64 bit Intel Xeon processor cores (12 cores processors) was used for the present simulation.

Geometry generation

The realistic geometry construction of the lung airway is challenging because of the highly complex anatomical arrangement of the lung. The geometrical structure of the human lung varies from person to person depending on age and health conditions. In recent years, several geometric improvement of the human lung have been conducted. In the case of modeling of particle TD in the lung, Weibel[3] lung model is still being used. Some anatomical developments of the idealized lung model were conducted to overcome its complexity.[11,12,46] In this study, the human lung geometry from a healthy person has been extracted from a CT image. The de-identified DiCom images of a healthy adult lung are used to extract the 3-D anatomical model. The normal CT DiCom images of 51 years healthy male were taken from near the larynx.

There are several steps are followed to develop the geometry from CT DiCom images. Firstly, de-identified CT scan DiCom data from a healthy individual has been collected from a local hospital (The Prince Charles Hospital, Brisbane, Australia). Secondly, the visualization and geometry generation software AMIRA are used to visualize the raw data. Figure 2(a) shows the raw CT data cross-sectional image and Figure 2(b) represents the cross-section of the row CT data with volren. Figure 2(c) shows the lung airway with the skeleton. To show the airway lung image, appropriate threshold and volren properties are used.

The third step is to extract the 3-D model from the CT images and the commencement of surface reconstruction. Figure 2(d) shows the image of lung lobes and airway geometry with the lobes. Some missing surface appears on the lung airway during the surface rendering. Geometry generation software GEOMAGIC is used for the surface rendering and redevelopment of the missing surface. After proper surface rendering and reconstruction, the final 3-D geometry of the lung airways has been created. Figure 2(e) is the final 3-D model of the lung airway. This study considered only the single bifurcation of the upper airway (Figure 2(e)).

Mesh generation

The lung geometry (Figure 2(e)) is not symmetric and consists of complex geometrical shapes. An unstructured tetrahedral mesh (Figure 3(a)) has been generated for the upper airway model. Due to the enormous number of elements, the tetrahedral elements are not clearly visible. Inflation layer mesh is generated for better near wall mesh treatment. The inflation layer elements are assigned as hexahedral to explain the complex flow field near to the wall. The transition ratio of the inflation is 0.202, and the growth rate is 1.3.

Figure 3(b) and (c) shows the inflation layer mesh at the wall and the inlet respectively. To generate a finer mesh, advance size function on curvature and proximity is used, and the maximum face size of the mesh is set to 0.00031225. To investigate the airflow at the carinal angle of the lung geometry, a fine tetrahedral cells are generated at the carinal angle area. The minimum orthogonal quality of the generated mesh is 0.19. The residual convergence criteria for the mesh convergence test is used as 0.0001.

Grid independent test

A grid refinement test for the generated mesh is investigated. Seven different sets of elements are constructed for the mesh independent test. Figure 4 represents the grid independence test results for dynamic pressure at the outlet, velocity magnitude at the inlet, and the deposition efficiency (DE) respectively. The grid refinement test results illustrate that the solution for different parameters are getting stable at 7.2 million elements, which theoretically declare that the present 7.2 million computational elements
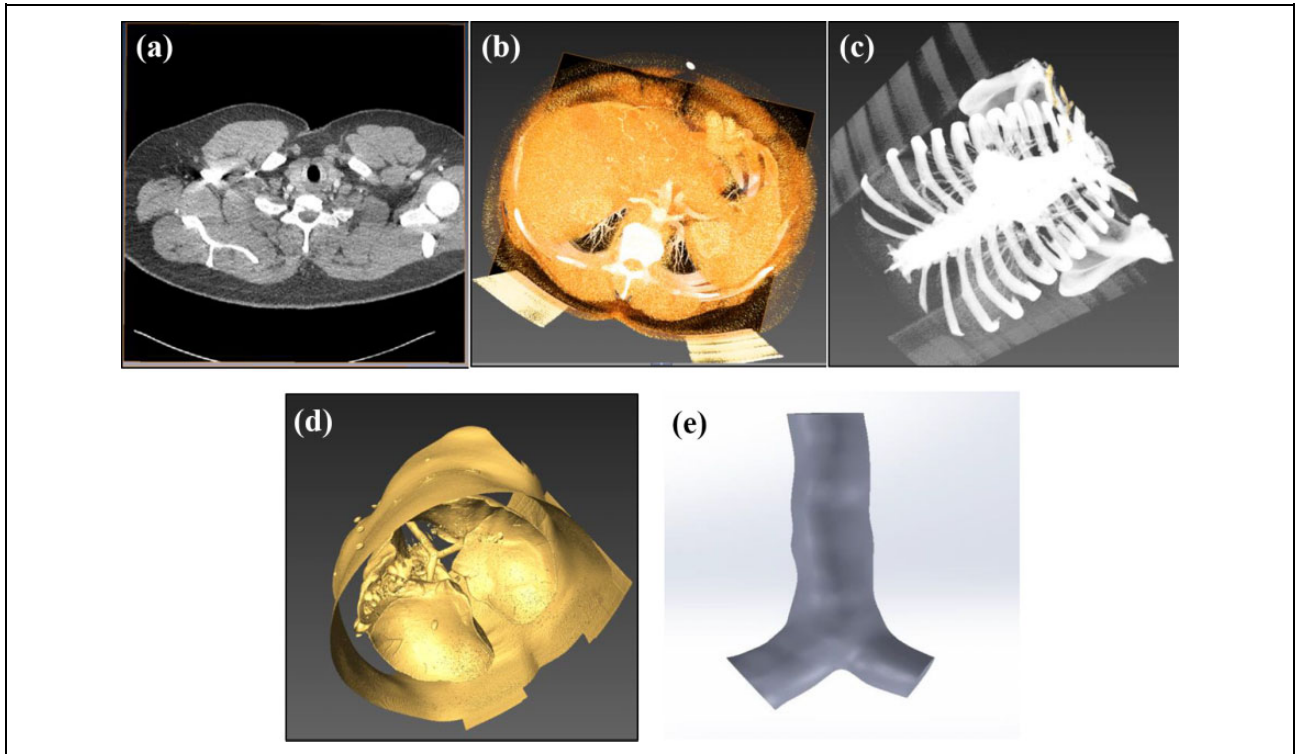
Figure 2. (a) Raw CT image and cross-sectional view, (b) cross-sectional view with volren, (c) image of lung airway with the skeleton, (d) image of lung lobes, and (e) 3-D anatomy of the lung for the central airway. CT: computed tomography.
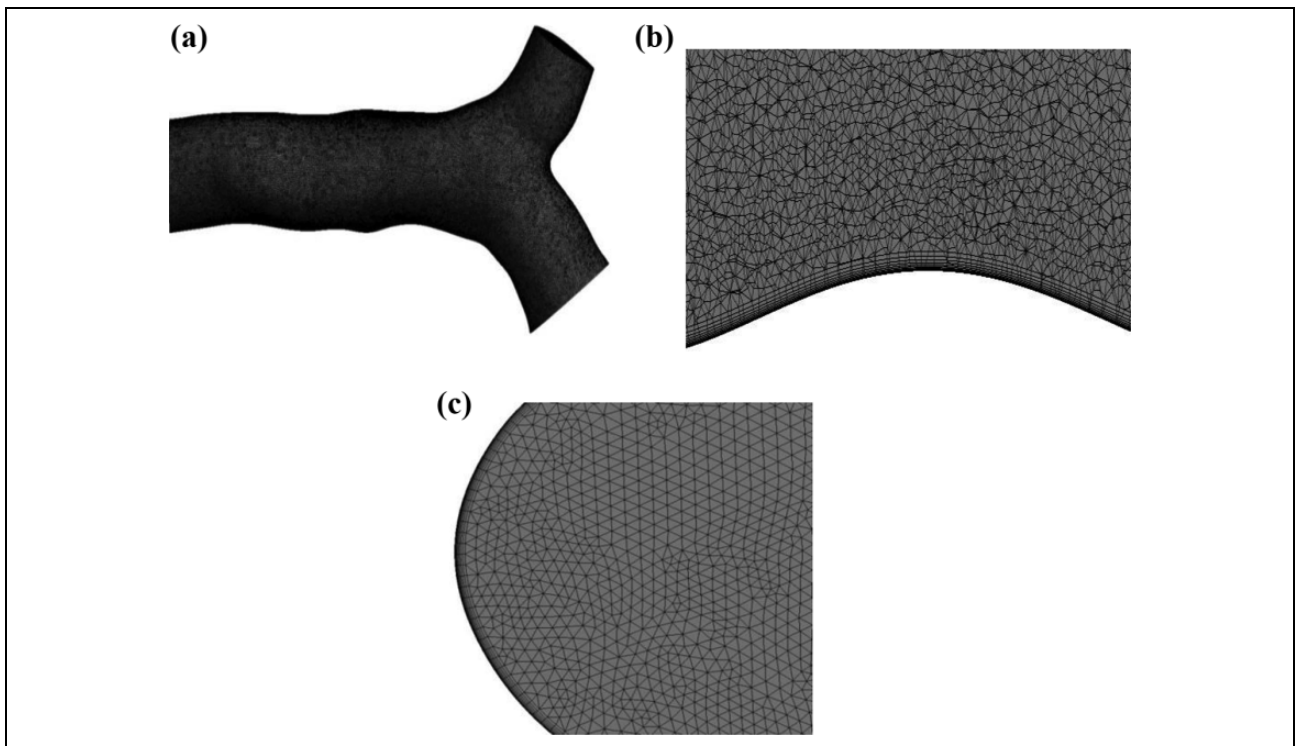

Figure 3. (a) Generated tetrahedral mesh for upper airway (mesh cells are not visible as it contains large number of cells), (b) inflation layer mesh, and (c) sectional view of the inlet mesh.
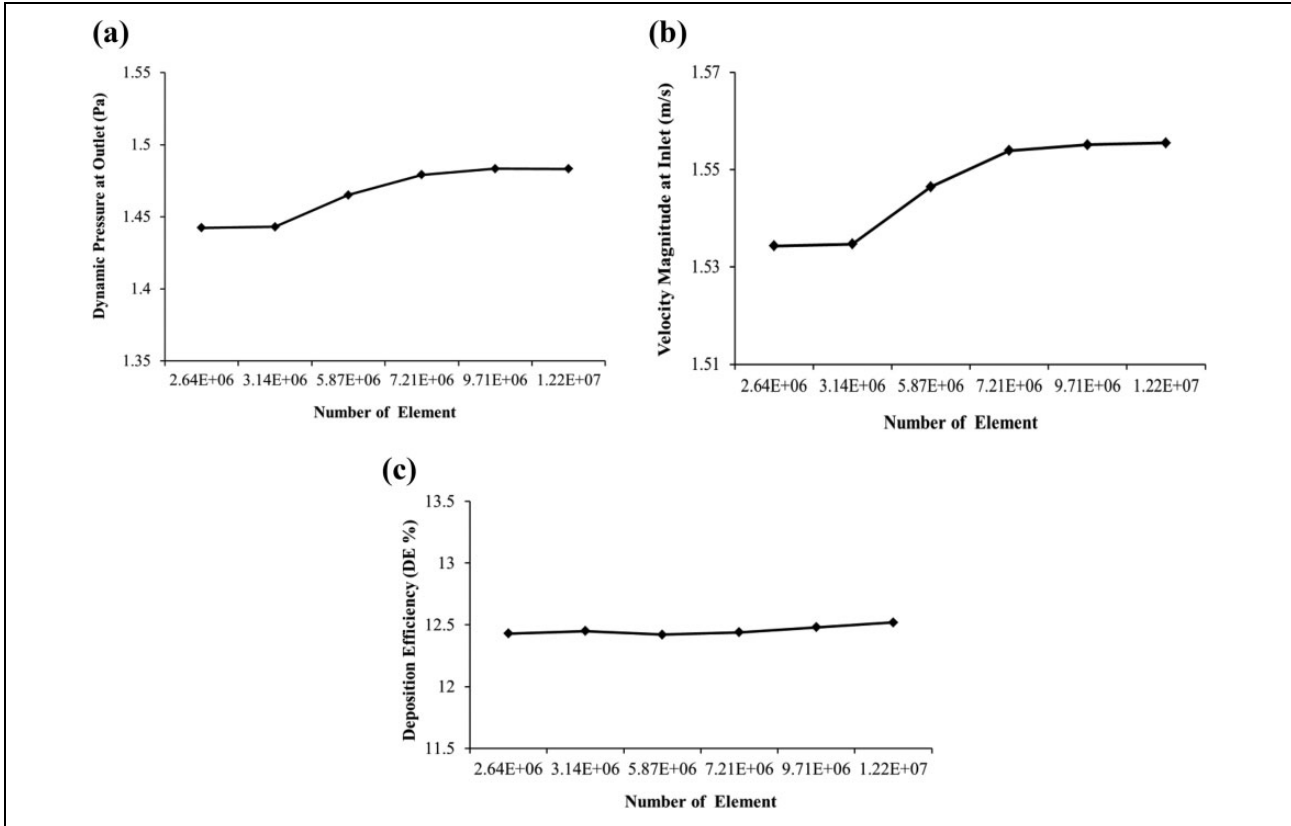
Figure 4. Grid independent test results of generated mesh for (a) dynamic pressure at the outlet, (b) velocity magnitude at the inlet, and (c) grid independent test for the DE. DE: deposition efficiency.

are sufficient to calculate the particle TD in the single bifurcation model of the human lung airway.

A comprehensive validation has been performed, which can be found in the supplementary section.

Result and discussion

Different geometrical model

To investigate the anatomical shape effects on aerosol particle TD, the well-established Weibel's symmetrical model, asymmetric modified CT model, and CT-based lung model dimensions are used to generate the geometry of the central airway of the human lung. In the case of modified CT lung model, the lung wall surface is kept as smooth as Weibel's symmetrical lung model. The extracted 3-D realistic model is highly complex in structure with uneven curves and bends all over the surface. Microparticle TD in the central airway of the three different anatomical models are investigated. Table 1 shows the summary of the CT-based lung model dimensions, Reynolds number and Stokes number in the current model. The hydraulic diameter of the noncircular inlet and the outlet of the realistic lung are measured.

The velocity profile along the selected line of the tracheal tube is plotted for different anatomical models. Figure 5 shows the velocity profile for 60 l/min flow rate. The calculated profile at the tracheal airway for idealized

Table 1. Computational domain dimensions and parameters.

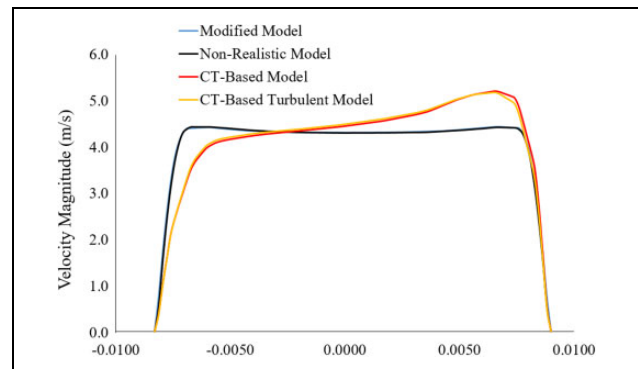|	
Trachea length (mm)	63.420
Inlet hydraulic diameter (mm)	18.626
Right branch length (mm)	24.978
Right branch hydraulic diameter (mm)	14.633
Left branch length (mm)	23.116
Left branch hydraulic diameter (mm)	13.684

Figure 5. Velocity profile at the selected line of the tracheal inlet for different anatomical model.

model and modified idealized model reports no velocity difference, while the velocity profile for CT-based model shows velocity difference near the tracheal wall. The
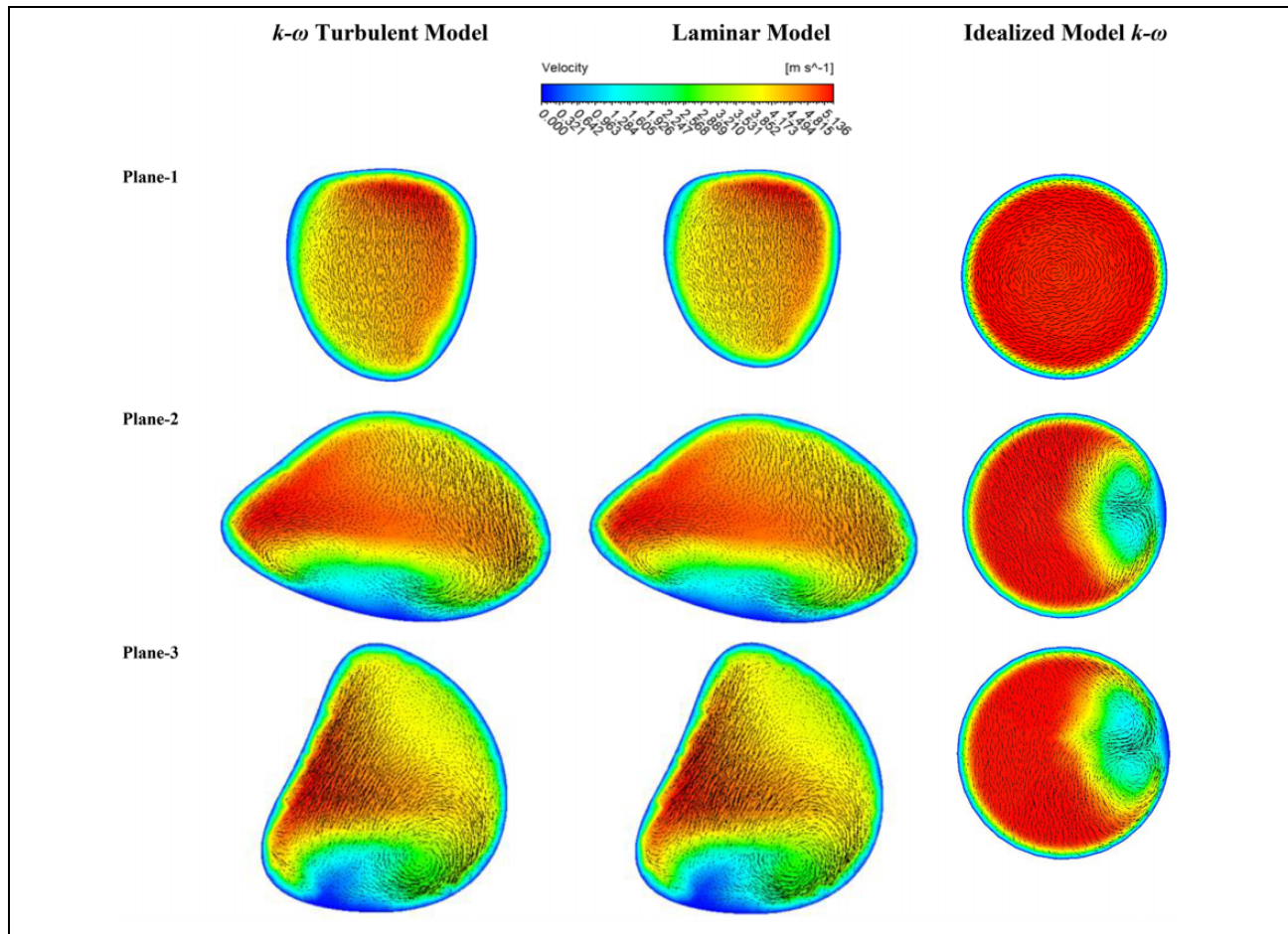
Figure 6. Velocity contour comparison at different planes of realistic and nonrealistic model for laminar and turbulent model.

velocity profile at the selected line for turbulent and laminar models are investigated and the velocity profile shows negligible fluctuation along the line.

For better understanding of the flow field for CT-based anatomical model, velocity contours at the different planes are calculated. Figure 6 shows the velocity contours at 60 l/min flow rate for laminar and k–ω turbulent model. The velocity contour is presented along with the velocity vector and the contour at the tracheal region (plane 1) for both model shows a similar velocity field. Plane 2 and plane 3 present the velocity contour at the right and the left airway, respectively, and report a negligible turbulence fluctuation variation for both models like the velocity profile presented in Figure 5. For nonrealistic model, the velocity field at the tracheal area is found fully developed and the flow field becomes complex at the bronchioles.

Figure 7 reports the respiratory deposition for 10-μm diameter particles at fast breathing pattern for different lung models. Figure 7(a) to (c) depicts the spherical particle deposition for Weibel's, modified, and realistic geometry, respectively. Figure 7(d) to (f) presents the NS particle deposition pattern for the same geometry configurations. The Weibel's and modified CT geometry show that the deposition density is profound at the carinal angle and the

bifurcation area. As mentioned in the literature review that the area near the bifurcation angle is the hot spot for deposition for nonrealistic geometry. On the contrary, the 3-D realistic geometry of the central airway reveals a new deposition hot spot (DHS) for particle deposition. The deposition scenario demonstrates that the deposition concentration is dominant at the lung tracheal wall compared with the carinal angle. The present particle TD scenario of the realistic CT lung model clearly differ from the previously published study based on the nonrealistic lung model. As the nonrealistic model showed good agreement with the published nonrealistic model, this may infer that the previously published nonrealistic models are unable to demonstrate the realistic particle deposition scenario in the lung airway. Recently, Mead-Hunter et al.[47] also showed the similar types of deposition pattern at the central airways for CT-based Sprague-Dawley rat model, which also support the findings of the present realistic lung model. The anatomical structure of the airways, particle diameter, and flow rates play an important role for the aerosol deposition. At the very upper airway, inertial impaction is the main tool for deposition irrespective to the anatomical structure of the lung. The microparticle inertia has a main role for particle deposition at the bifurcating angle of the nonrealistic lung
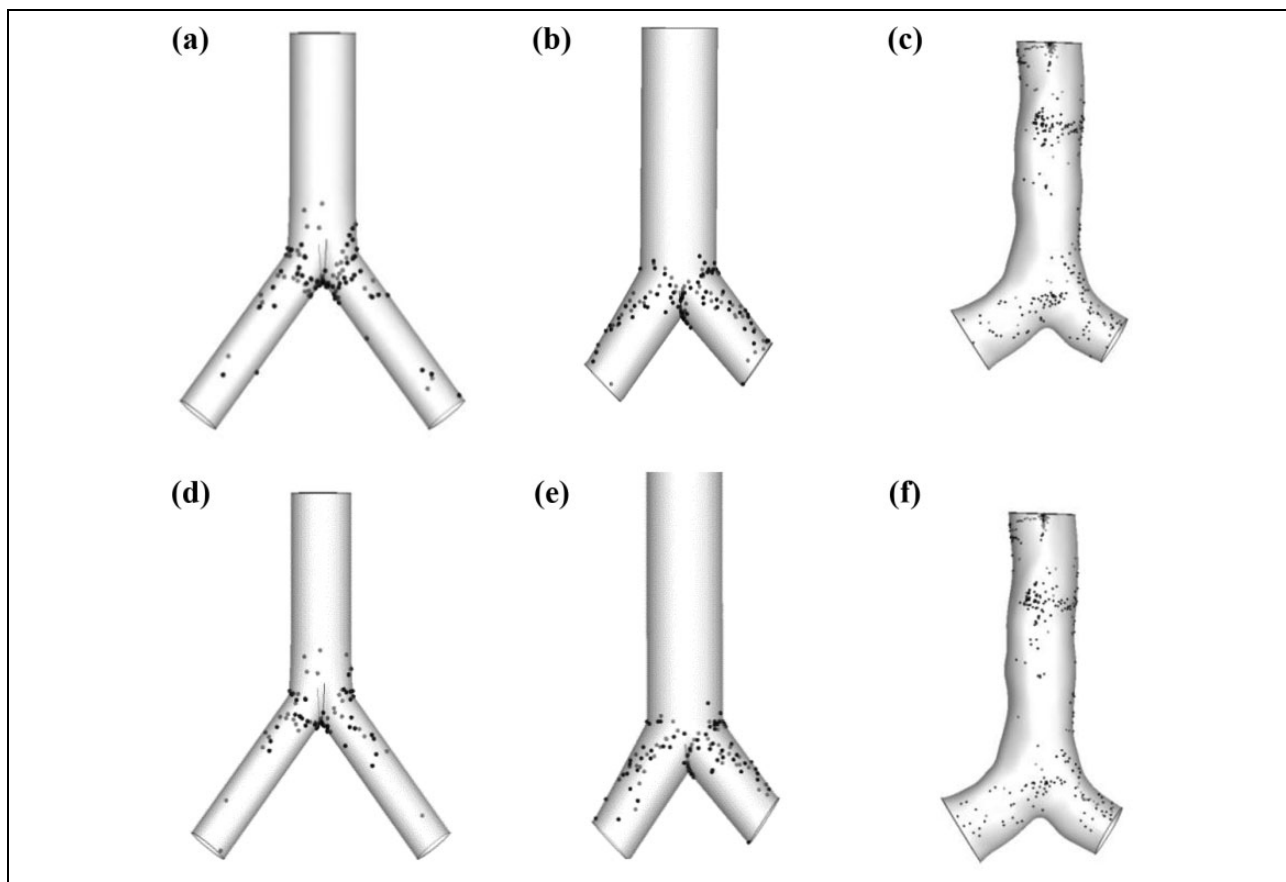
Figure 7. Respiratory deposition pattern of 10-μm diameter particle at the fast breathing pattern: (a) Weibel's lung model—spherical, (b) Modified CT lung model—spherical, (c) CT scan lung model—spherical, (d) Weibel's lung model—NS, (e) modified CT lung model—NS, and (f) CT scan lung model—NS. NS: nonspherical; CT: computed tomography.

geometry. Particle usually follows the air streamline during the movement. Larger particles cannot monitor the air streamline if there presents any curvature, bending, or obstruction. As a result, particles diverge from the air stream and get in contact with the obstruction. For nonrealistic geometry, particles only interact with the bending wall at the carinal angle, and that is the reason the bifurcation area is the DHS. On the contrary, for the CT scan-based realistic lung airway, when particles with considerable inertia encounter any barrier on its way at a higher flow rate, the particles stray from the streamline and interact with the barrier. This explains the higher particle deposition concentration along the walls of a CT geometry based lung airway.

Turbulent effects on aerosol particle TD is investigated for 60 l/min flow rate. Table 2 shows the calculated deposition efficiency for different diameter particle. The overall calculation shows a negligible DE difference (less than 2%) for laminar and k–ω turbulent cases at the upper airways. The DE for nonrealistic model is found significantly lower than the realistic model.

To analyze the DHS more comprehensively in the three different lung geometries, the deposition density curves for the deposited particles are investigated. Figure 8 illustrates

Table 2. DE of different diameter particles at 60 l/min flow rate.

	1 μm	5 μm	10 μm
Nonturbulent model	28.1	34.5	43.1
k–ω turbulent model	27.26	32.51	41.9
Nonrealistic k–ω model	1.7	2.79	12.97

DE: deposition efficiency.

the deposition density of the spherical particles at different breathing conditions. Figure 8(a) demonstrates the deposition density of the different diameter spherical particles during slow breathing pattern. Figure 8(b) and (c) shows the spherical particles deposition density comparison in Weibel's and modified lung geometry, respectively. The deposition density curve reports that the bifurcation area is the DHS for both Weibel's and modified lung geometries, regardless the particle diameter and breathing pattern. The previously published results of Russo et al.[48] also support the present result. Russo et al.[48] also calculated the percentage of deposition at different portions of their smooth and ringed like geometry for the central airway and found a similar deposition concentration in the bifurcation area. Figure 8(a) to (c)
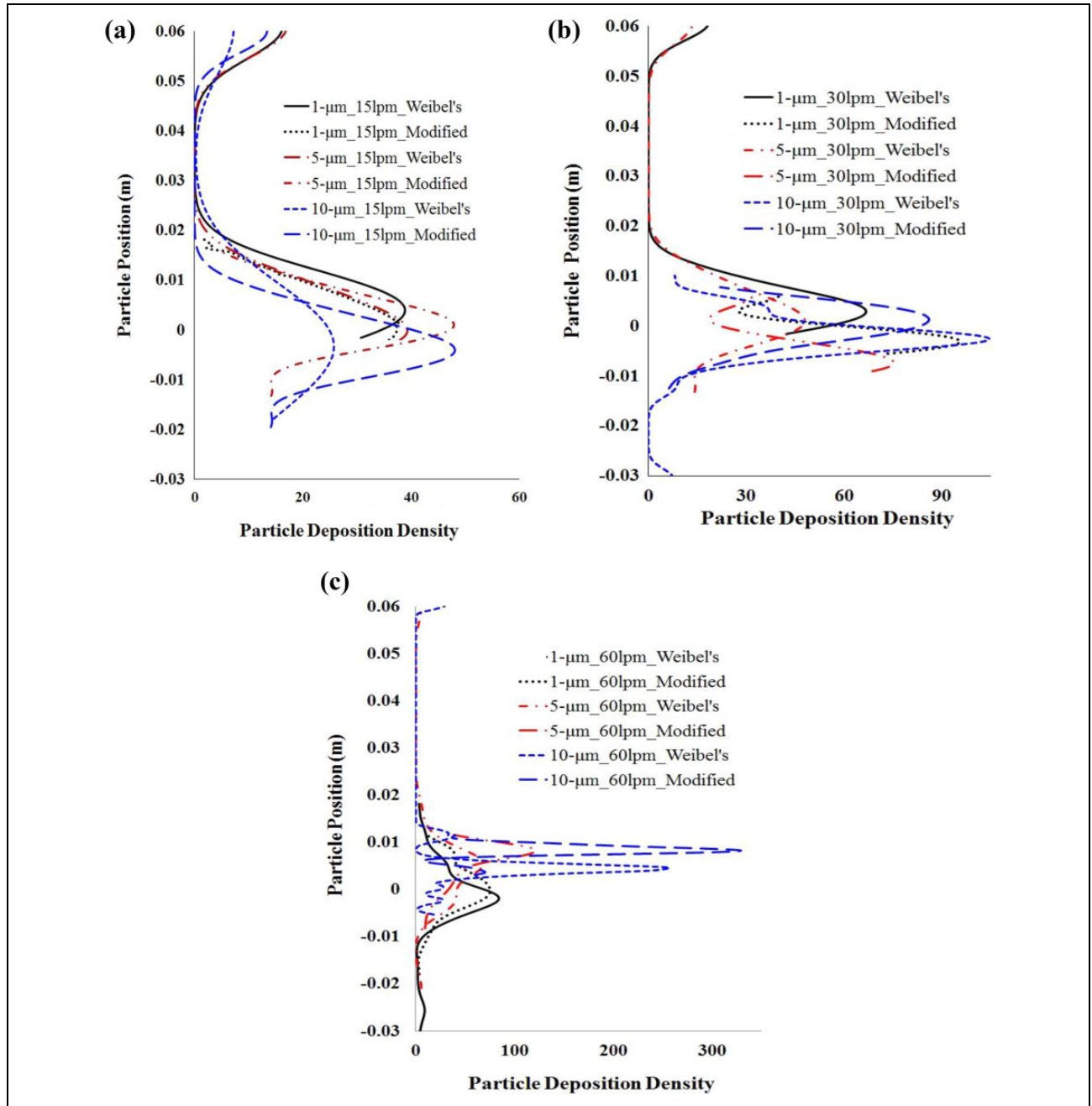
Figure 8. The deposition concentration comparison of spherical particles at different parts of the central airway of Weibel's and modified lung geometry: (a) 15 l/min, (b) 30 l/min, and (c) 60 l/min flow rates.

also reports concentration of the 10-µm particle in the bifurcation area is noticeably higher than the 5-µm and 1-µm particles. The inertia of the larger diameter particle and higher flow rate increases the DE at the bifurcation angle than the smaller diameter particle. Particles with large inertia are unable to follow the curved streamline; consequently, these particles will hit the wall of the carinal angle. The curve shows that the deposition density in the bifurcation areas increases with particle diameter irrespective of the flow rate.

Figure 9(a) to (c) reports the NS particle deposition density for different diameter particles. The NS particle density curve shows a similar DHS similar to the spherical one. The density curve illustrates that the deposition density of the 10-µm NS particle in the bifurcation area of the modified geometry is greater than the Weibel's geometry regardless of the flow rate. The modified lung model is geometrically asymmetric, explaining why NS microparticles' aspect ratio and large inertia acts a significant role in the deposition in the bifurcation area.
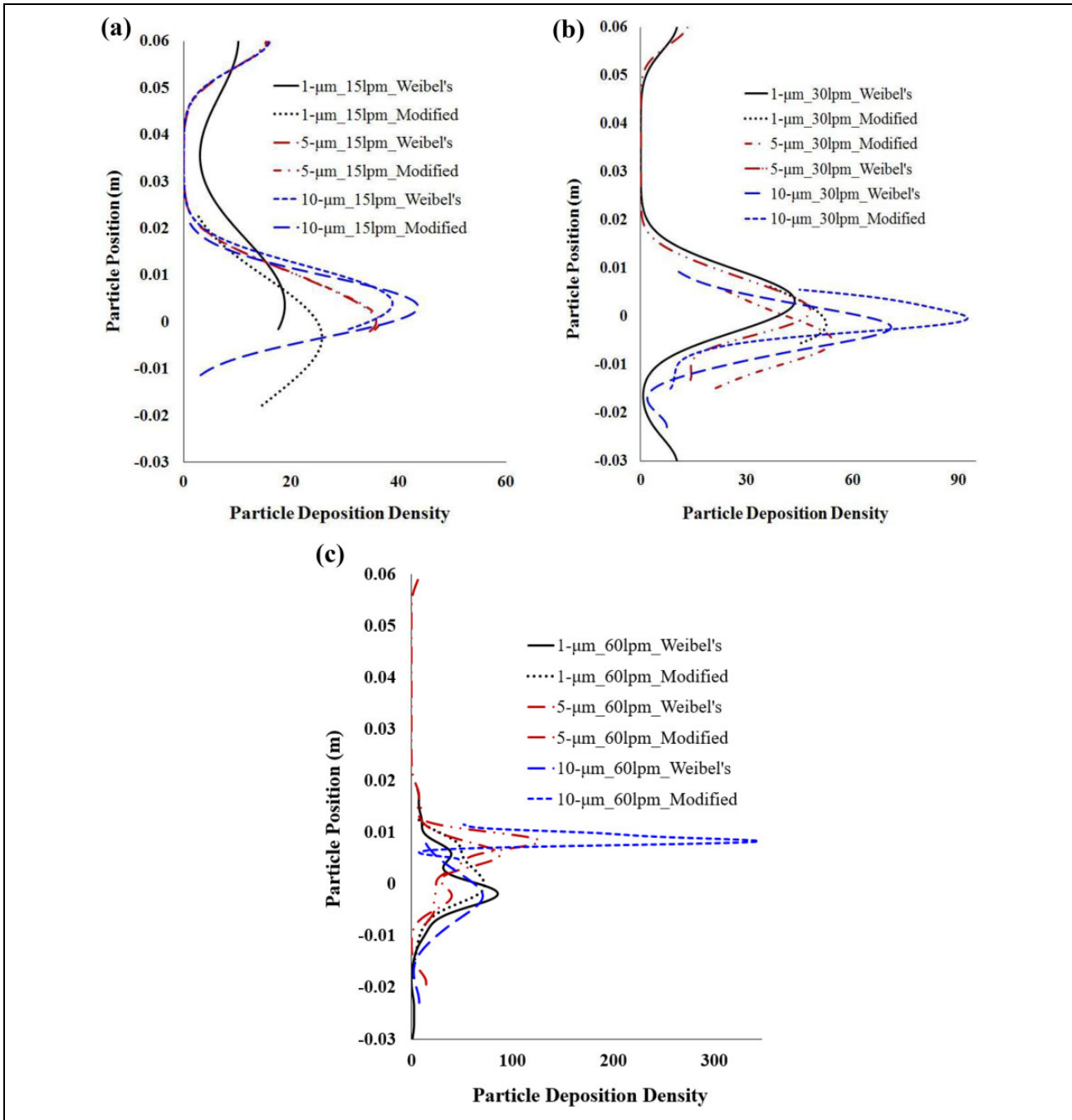
Figure 9. The deposition density comparison of the NS particle at the different part of the central airway of Weibel's and modified lung geometry: (a) 15 l/min, (b) 30 l/min, and (c) 60 l/min flow rates. NS: nonspherical.

Figure 10(a) to (c) illustrates a comparative assessment of the deposition densities of spherical and NS particle at different regions of the central airway of the realistic lung geometry at 15l/min, 30 l/min, and 60 l/min flow rates, respectively. The overall deposition density curve demonstrates the DHS at the upper section of the trachea and the bifurcation area. The ordinate values of the nonrealistic and realistic anatomical models are different due to the different coordinate's representation. The vertical axis values in the density curve correspond to the *y*-coordinate for the

symmetric model and the *z*-coordinate for the realistic model. Figure 10(a) shows the deposition density at the upper part of the trachea decreases with decreasing particle diameter at 15 l/min flow rate. Figure 10(c) also shows a similar deposition pattern for spherical and NS particle during the fast breathing pattern. The deposition density curve shows the DHS is in the upper section and the bifurcation area of the central airway. The deposition scenario also shows that NS particle deposition density at the upper section of the trachea is higher than that of the spherical
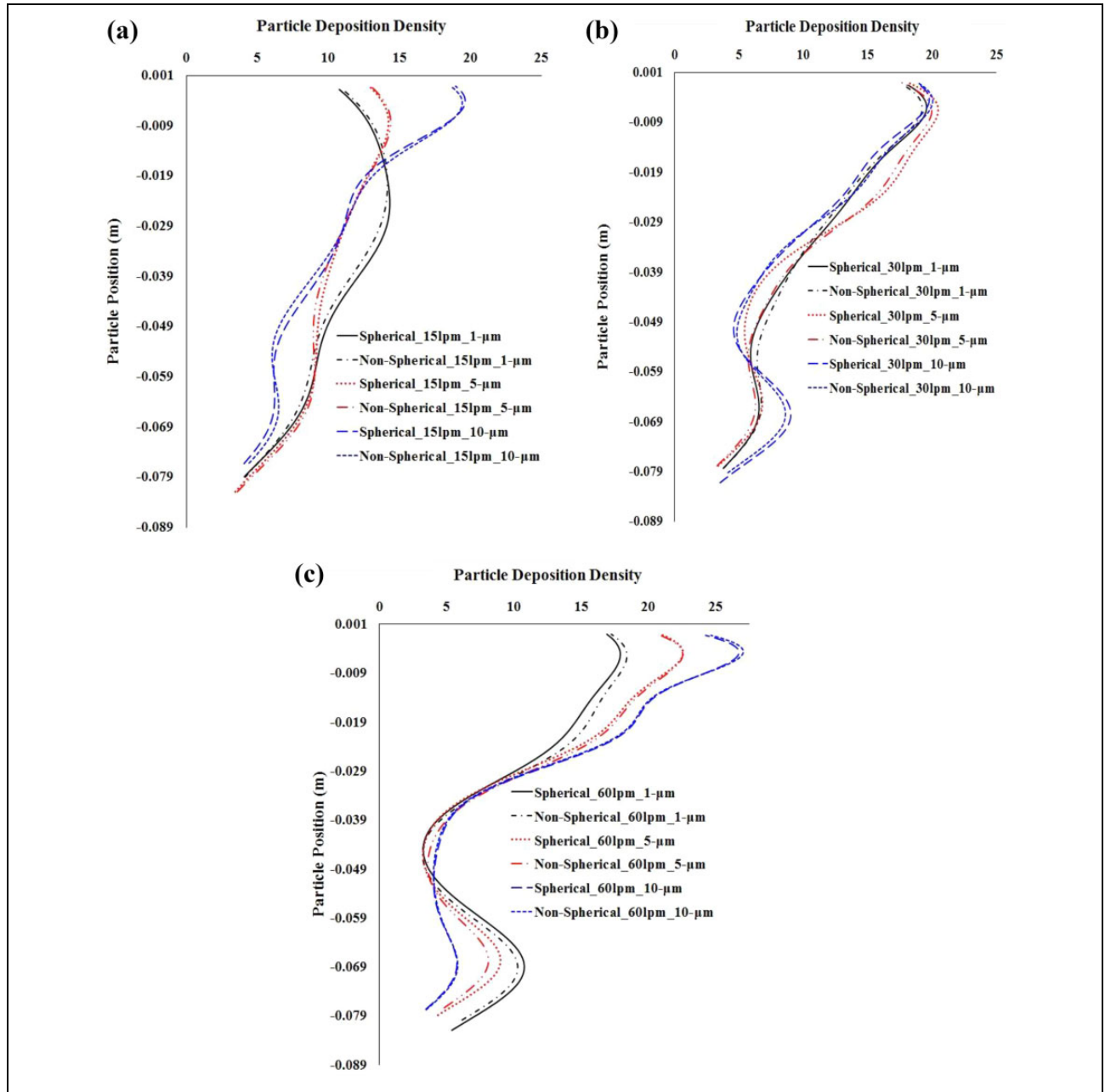
Figure 10. The deposition comparison of the spherical and NS particle at the different part of the central airway of realistic lung geometry: (a) 15 l/min, (b) 30 l/min, and (c) 60 l/min flow rates. NS: nonspherical.

one. Figure 10(b) and (c) shows the spherical particle deposition concentration in the bifurcation area is higher than that of the NS particle, whereas Figure 10(a) shows an opposite scenario in the bifurcation area. The 3-D realistic geometry asymmetricity and particle aspect ratio are responsible for these types of deposition pattern in the central airway.

Figure 11(a) and (b) shows the DE comparison for spherical and NS particle at different flow rates. Figure 11(a) shows the DE of the spherical particle for different lung geometry. The Weibel's, modified, and CT scan-based lung geometries show the DE increases with the increasing values of the flow rates irrespective of particle diameter.

Figure 11(b) shows a similar deposition pattern for the NS particle. The overall DE comparison shows the DE of the spherical and NS microparticle in realistic lung geometry is significantly higher than the nonrealistic geometry.

Table 3 shows the summary of the escaped particles through the two bifurcation branches. The particle transport history indicates that a significant amount of particles have gone through the daughter bronchioles, which would then enter the 2nd bifurcation of the airways. In reality, those particles could travel the rest of the downstream generation after the second generation to the 23rd generation in a whole lung model. Depending on the size
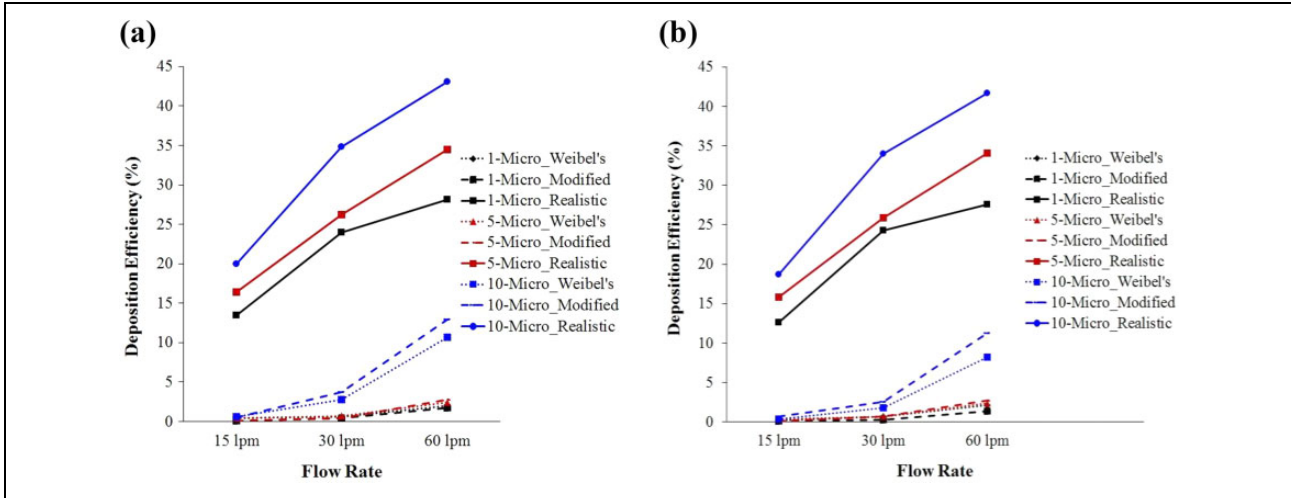
Figure 11. Respiratory DE comparison for Weibel's, modified, and realistic lung geometry for (a) spherical particle and (b) NS particle. NS: nonspherical; DE: deposition efficiency.

Table 3. Spherical and NS particle transport summary toward the next generation in three different lung model.

| Weibel's geometry						Modified geometry						Realistic geometry					
Spherical			NS			Spherical			NS			Spherical			NS		
1 μm	5 μm	10 μm	1 μm	5 μm	10 μm	1 μm	5 μm	10 μm	1 μm	5 μm	10 μm	1 μm	5 μm	10 μm	1 μm	5 μm	10 μm
15 lpm 99.6	99.6	99.4	99.8	99.6	99.6	99.9	99.9	99.5	99.9	99.9	99.3	86.5	83.6	80.0	87.4	84.2	81.3
30 lpm 99.4	99.3	97.2	99.3	99.3	98.2	99.6	99.6	96.3	99.3	99.3	97.4	76.0	73.8	65.2	75.7	74.0	66.0
60 lpm 98.0	97.6	89.3	97.9	97.6	91.8	98.3	97.2	86.9	98.6	97.3	88.7	71.9	65.5	56.9	72.4	65.9	58.3

NS: nonspherical.
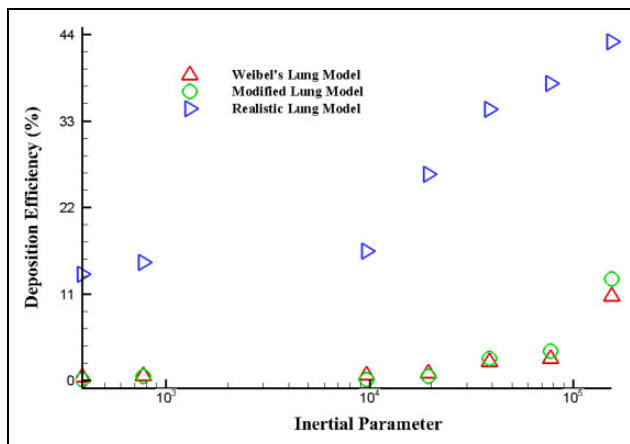
Figure 12. First bifurcation DE comparison for different lung model against the inertial parameter, $\rho d_p^2 Q$ (g μm² s⁻¹). DE: deposition efficiency.

distribution, smaller particles could pass into the alveolar sacs, and finally, the particles could get access to the blood of the body.

Figure 12 depicts that the DE for different lung model is relative to the inertial parameter $\rho d_p^2 Q$, which also indicates that impaction is the leading mechanism at the central airways of the lung.

Conclusions

In this study, the TD of microparticles ranging from $1 \leq d_p \leq 10$ μm in the idealized and realistic lung have been investigated. A numerical framework is developed to calculate the coal-mine exhaust microparticle TD in human lung airways. The numerical simulations have been conducted at different flow rates. The 3-D geometry of a healthy human lung airway was developed from the CT images. The following conclusions are drawn from the study:

- New DHS is observed for the realistic geometry of the central airway. The deposition pattern shows that most of the aerosol particles are deposited on the tracheal wall instead of the carinal angle.
- Different DHS is observed based on the fluid flow rate. In case of a lower flow rate, particle concentration was mostly higher in the middle of the trachea. In the case of higher flow rate, the particle

concentration was significant in the upper section and the bifurcation area.

- The coal exhaust particle diameter and fluid flow rate influence the deposition pattern. The DE increases with the flow rate and particle size.
- Particle shape influences the deposition pattern. The deposition density curve clearly showed that higher number of NS particles was deposited on the upper section compare to the spherical particle.

The findings of the present study for CT-based realistic lung geometry would benefit the pharmaceutical industry to design the drug delivery systems to the respiratory airways. As the realistic lung airway shows a new deposition pattern, the present finding may be used to develop a more realistic therapeutically targeted medication transport system for the respiratory tract. The current particle transport data for the CT-based central airway and further investigation of more distal airway generations would give a clear idea about the pharmaceutical aerosol transport to the transitional airways of the lung. The new deposition pattern for realistic lung model differs from the available *in silico* model. This is an important improvement for the understanding of the more realistic zone specific drug delivery system. The present study, together with a more comprehensive study on the size-specific particle TD at the more distal airways of the realistic lung geometry, will provide clinically and biologically relevant models of targeted drug delivery systems into the lungs. These models would guide the development and testing of novel therapies for lung disease, including inhaled bronchodilators, anti-inflammatory agents, antibiotics, and replacement therapies. The comprehensive particle TD investigation for more generation of CT-based lung airway (based on CT data resolution) for size-specific polydispersed particle will be the next study to improve the knowledge of the targeted drug delivery system in the deeper airways. The future study will also consider more realistic sample for healthy and diseased lung for better prediction of particle TD.

Nomenclature

TD: transport and deposition	$\vec{g}$: gravitational body force
CT: computed tomography	$\vec{F}$: external body forces
E-L: Euler–Lagrange	I: unit tensor
EDM: effective diameter method	μ: dynamic viscosity
DHS: deposition hot spot	F_D: drag force
LPT: Lagrangian particle tracking	ρ_P: particle density
NS: nonspherical	d_p: particle diameter
DPM: discrete phase model	R_e: Reynolds number
UDF: user-defined function	C_D: drag coefficient
DE: deposition efficiency	A_s: surface area of sphere
S_m: source mass	A_P: surface area of particle
p: static pressure	Ψ: shape factor

ORCID iD

Mohammad S Islam https://orcid.org/0000-0001-6264-3886
Suvash C Saha https://orcid.org/0000-0002-9962-8919

Supplemental material

Supplemental material for this article is available online.

References

1. Tena A and Casan Clarà P. Deposition of inhaled particles in the lungs. *Arch Bronconeumol* 2012; **48**(7): 240–246.
2. Watson H. Dust sampling to simulate the human lung. *Br J Ind Med* 1953; **10**(2): 93.
3. Weibel ER. *Morphometry of the human lung*. New York: Springer Verlag and Academic Press, 1963.
4. Zhang Z and Kleinstreuer C. Laminar-to-turbulent fluid–nanoparticle dynamics simulations: model comparisons and nanoparticle-deposition applications. *Int J Numer Method Biomed Eng* 2011; **27**(12): 1930–1950.
5. Kannan R, Guo P and Przekwas A. Particle transport in the human respiratory tract: formulation of a nodal inverse distance weighted Eulerian–Lagrangian transport and implementation of the Wind–Kessel algorithm for an oral delivery. *Int J Numer Method Biomed Eng* 2016; **32**(6): e02746.
6. Rahimi-Gorji M, Gorji TB and Gorji-Bandpy M. Details of regional particle deposition and airflow structures in a realistic model of human tracheobronchial airways: two-phase flow simulation. *Comput Biol Med* 2016; **74**: 1–17.
7. Rahimi-Gorji M, Pourmehran O, Goriji-Bandpy M, et al. CFD simulation of airflow behavior and particle transport and deposition in different breathing conditions through the realistic model of human airways. *J Mol Liq* 2015; **209**: 121–133.
8. Aslett E, Hart AA and McMichael J. The lung volume and its subdivisions in normal males. *Proc R Soc Lond Ser B Biol Sci* 1939; **126**: 502–528.
9. Briscoe WA and Dubois AB. The relationship between airway resistance, airway conductance and lung volume in subjects of different age and body size. *J Clin Invest* 1958; **37**(9): 1279.
10. Horsfield K and Cumming G. Morphology of the bronchial tree in man. *J Appl Physiol* 1968; **24**(3): 373–383.

11. Raabe OG, Yeh HC, Schum GM, et al. *Tracheobronchial geometry: human, dog, rat, hamster*. Lovelace Foundation for Medical Education and Research, 1976.

12. Horsfield K, Dart G, Olson DE, et al. Models of the human bronchial tree. *J Appl Physiol* 1971; **31**(2): 207–217.

13. Koblinger L and Hofmann W. Monte Carlo modeling of aerosol deposition in human lungs. Part I: Simulation of particle transport in a stochastic lung structure. *J Aerosol Sci* 1990; **21**(5): 661–674.

14. Balásházy I and Hofmann W. Particle deposition in airway bifurcations–II. Expiratory flow. *J Aerosol Sci* 1993; **24**(6): 773–786.

15. Asgharian B, Hofmann W and Bergmann R. Particle deposition in a multiple-path model of the human lung. *Aerosol Sci Technol* 2001; **34**(4): 332–339.

16. Islam MS, Saha SC, Sauret E, et al. Numerical investigation of aerosol particle transport and deposition in realistic lung airway. In: *Proceedings of the international conference on computational methods*, Auckland, New Zealand, 14–17 July 2015. Berkeley: Scientech Publisher.

17. Cebral JR and Summers RM. Tracheal and central bronchial aerodynamics using virtual bronchoscopy and computational fluid dynamics. *IEEE Trans Med Imaging* 2004; **23**(8): 1021–1033.

18. Kvasnak W and Ahmadi G. Fibrous particle deposition in a turbulent channel flow—an experimental study. *Aerosol Sci Technol* 1995; **23**(4): 641–652.

19. Yu C. Exact analysis of aerosol deposition during steady breathing. *Powder Technol* 1978; **21**(1):55–62.

20. Chen X, Zhong W, Sun B, et al. Study on gas/solid flow in an obstructed pulmonary airway with transient flow based on CFD–DPM approach. *Powder Technol* 2012; **217**: 252–260.

21. Kannan R, Chen ZJ, Singh N, et al. A quasi-3D wire approach to model pulmonary airflow in human airways. *Int J Numer Method Biomed Eng* 2017; **33**(7): e2838.

22. Oakes JM, Shadden SC, Grandmont C, et al. Aerosol transport throughout inspiration and expiration in the pulmonary airways. *Int J Numer Method Biomed Eng* 2017; **33**(9): e2847.

23. Sanmiguel-Rojas E, Burgos MA, Del Pino C, et al. Robust nondimensional estimators to assess the nasal airflow in health and disease. *Int J Numer Method Biomed Eng* 2018; **34**(1): e2906.

24. Islam MS, Saha SC, Gemci T, et al. Euler-Lagrange prediction of diesel-exhaust polydisperse particle transport and deposition in lung: anatomy and turbulence effects. *Sci Rep* 2019; **9**(1): 12423.

25. Rahimi-Gorji M, Debbaut C, Van de Sande L, et al. Computational model of pressurized intraperitoneal chemotherapy (PIPAC) for carcinomatosis treatment. In: *OncoPoint 2019*. 2019.

26. Bagheri G and Bonadonna C. On the drag of freely falling non-spherical particles. *Powder Technol* 2016; **301**: 526–544.

27. Kasper G. Dynamics and measurement of smokes. I Size characterization of nonspherical particles. *Aerosol Sci Technol* 1982; **1**(2): 187–199.

28. Wen H and Kasper G. Dynamics and measurement of smokes III—drag and orientation of chain aggregates in an electrical mobility spectrometer. *Aerosol Sci Technol* 1984; **3**(4): 397–403.

29. Kasper G and Wen HY. Dynamics and measurement of smokes IV—comparative measurements with an aerosol centrifuge and an aerodynamic particle sizer APS33 using submicron chain aggregates. *Aerosol Sci Technol* 1984; **3**(4): 405–409.

30. Fan F-G and Ahmadi G. A sublayer model for wall deposition of ellipsoidal particles in turbulent streams. *J Aerosol Sci* 1995; **26**(5): 813–840.

31. Zhang H, Ahmadi G, Fan F-G, et al. Ellipsoidal particles transport and deposition in turbulent channel flows. *Int J Multiph Flow* 2001; **27**(6): 971–1009.

32. Kleinstreuer C and Feng Y. Computational analysis of nonspherical particle transport and deposition in shear flow with application to lung aerosol dynamics—a review. *J Biomech Eng* 2013; **135**(2): 021008.

33. Zhong W, Yu A, Liu X, et al. DEM/CFD-DEM modelling of non-spherical particulate systems: theoretical developments and applications. *Powder Technol* 2016; **302**: 108–152.

34. Feng Y and Kleinstreuer C. Analysis of non-spherical particle transport in complex internal shear flows. *Phys Fluids* 2013; **25**(9): 091904.

35. Wadell H. The coefficient of resistance as a function of Reynolds number for solids of various shapes. *J Franklin Inst* 1934; **217**(4): 459–490.

36. Li Q, Lin B, Zhao S, et al. Surface physical properties and its effects on the wetting behaviors of respirable coal mine dust. *Powder Technol* 2013; **233**: 137–145.

37. Islam MS, Saha SC, Sauret E, et al. Numerical investigation of diesel exhaust particle transport and deposition in up to 17 generations of the lung airway. In: 20th Australasian fluid mechanics conference, Perth, Australia, 5–8 December 2016.

38. Saha SC, Islam MS, Rahimi-Gorji M, et al. Aerosol particle transport and deposition in a CT-scan based mouth-throat model. In: *AIP conference proceedings 2121, 040011*, Melville, 2019. DOI: 10.1063/1.5115882.

39. Rahimi-Gorji M, Van de Sande L, Debbaut C, et al. Computational fluid dynamics model of pressurized intraperitoneal aerosol chemotherapy: gravity matters! In: *SB3C2019-Summer biomechanics, bioengineering and biotransport conference*, Seven Springs, Pennsylvania, 25–28 June 2019.

40. Islam MS, Saha SC, Gemci T, et al. Polydisperse microparticle transport and deposition to the terminal bronchioles in a heterogeneous vasculature tree. *Sci Rep* 2018; **8**(1): 16387.

41. Islam MS, Saha SC, Sauret E, et al. Ultrafine particle transport and deposition in a large scale 17-generation lung model. *J Biomech* 2017; **64**: 16–25.

42. Islam MS, Saha SC, Sauret E, et al. Numerical investigation of diesel exhaust particle transport and deposition in the CT scan based lung airway. *AIP Conference Proceedings* **1851**(1); Article ID 020092 (2017). DOI: 10.1063/1.4984721.

43. Morawska L, He C, Hitchins J, et al. Characteristics of particle number and mass concentrations in residential houses in Brisbane, *Australia*. Atmos Environ 2003; **37**(30): 4195–4203.

44. Israel GW, Erdmann A, Shen J, et al. Methods to determine the origin of suspended particulate matter in ambient air. *Staub Reinhalt Luft* 1992; **52**(7): 283–291.

45. Tsuji Y. Multi-scale modeling of dense phase gas–particle flow. *Chem Eng Sci* 2007; **62**(13): 3410–3418.

46. Islam MS, Saha SC, Sauret E, et al. Pulmonary aerosol transport and deposition analysis in upper 17 generations of the human respiratory tract. *J Aerosol Sci* 2017; **108**: 29–43.

47. Mead-Hunter R, King AJ, Larcombe AN, et al. The influence of moving walls on respiratory aerosol deposition modelling. *J Aerosol Sci* 2013; **64**: 48–59.

48. Russo J, Robinson R, Oldham MJ, et al. Effects of cartilage rings on airflow and particle deposition in the trachea and main bronchi. *Med Eng Phys* 2008; **30**(5): 581–589.